Generation of transient dayside subauroral proton precipitation

S. A. Fuselier,[1] S. P. Gary,[2] M. F. Thomsen,[2] E. S. Claflin,[1] B. Hubert,[3] B. R. Sandel,[4] and T. Immel[5]

[1]   The Imager for Magnetopause-to-Aurora Global Exploration (IMAGE) spacecraft obtained the first global images of the proton aurora. One of the discoveries from these images was a region of proton precipitation equatorward of the nominal auroral oval. This precipitation can be observed for ~10 min immediately following a large solar wind pressure pulse. Various mechanisms have been proposed for producing this precipitation. This study focuses on one of the proposed mechanisms, the scattering and precipitation of protons due to interaction with electromagnetic ion cyclotron (EMIC) waves. Using data from the IMAGE spacecraft FUV and EUV imagers, in situ ring current data from the Los Alamos geosynchronous spacecraft, and in situ solar wind data from the ACE spacecraft, two features of the precipitation, the local time occurrence and limited latitudinal extent, are explained. The local time occurrence of the precipitation is correlated with the orientation of the pressure pulse front in the solar wind. The limited latitudinal extent of the emissions appears to be related to the interaction between the hot ring current protons and the cold plasmaspheric ions that gives rise to EMIC wave growth.   INDEX TERMS: 2455 Ionosphere: Particle precipitation; 2772 Magnetospheric Physics: Plasma waves and instabilities; 2768 Magnetospheric Physics: Plasmasphere; 2139 Interplanetary Physics: Interplanetary shocks; KEYWORDS: plasma instabilities, proton precipitation, wave/particle interactions

1.   Introduction

[2]   Although aurora generated by precipitation of energetic (approximately tens of keV) protons have been observed from the ground [e.g., *Ono et al.*, 1987], the first global images of proton-generated aurora were obtained from the Imager for Magnetopause-to-Aurora Global Exploration (IMAGE) spacecraft [*Burch*, 2000]. This spacecraft was launched into a polar, elliptical orbit in March 2000. During the first 3 years of observations the spacecraft apogee precessed over the north geographic pole, providing excellent viewing of the northern auroral region.

[3]   The spacecraft has a set of FUV imagers which image aurora in three separate passbands [*Mende et al.*, 2000]. These aurora are produced by proton and electron precipitation in the upper atmosphere. The unique ability to make simultaneous images of aurora created solely by proton precipitation and aurora created by a combination of proton and electron precipitation has produced new results in auroral and magnetospheric physics [see, e.g., *Mende et al.*, 2001].

[4]   One particularly interesting, new discovery is the presence of auroral arcs equatorward of the dayside auroral oval. These auroral arcs have been described as afternoon sector detached proton auroral arcs [*Burch et al.*, 2002], detached proton arcs [*Immel et al.*, 2002], dayside detached auroras [*Zhang et al.*, 2003], and subauroral proton flashes [*Hubert et al.*, 2003]. All of these descriptive terms identify common features of the phenomenon. In particular, the arcs occur equatorward of and separate from the nominal dayside proton auroral oval, and they are created entirely from precipitation of protons [*Immel et al.*, 2002; *Hubert et al.*, 2003; *Zhang et al.*, 2003]. (On the dayside the nominal proton auroral oval is produced by precipitation of protons that originate near the magnetopause.)

[5]   The persistence of the subauroral proton precipitation suggests two separate categories for the phenomenon. Some arcs persist for many tens of minutes to over an hour [*Burch et al.*, 2002; *Immel et al.*, 2002], while others appear abruptly and fade within 10 min of their initial occurrence [*Fuselier et al.*, 2001; *Zhang et al.*, 2003; *Hubert et al.*, 2003]. While the root generation mechanism for the proton precipitation might be the same [e.g., *Burch et al.*, 2002], the different durations suggest that two different processes drive the arc creation.

[6]   The initial appearance of the longer-duration subauroral arcs has been linked to changes in the interplanetary magnetic field (IMF) [*Burch et al.*, 2002]. When the IMF B_z

[1]Lockheed Martin Advanced Technology Center, Palo Alto, California, USA.
[2]Los Alamos National Laboratory, Los Alamos, New Mexico, USA.
[3]Institut d'Atmospherique et de Geophysique, Université de Liège, Liège, Belgium.
[4]Lunar and Planetary Laboratory, University of Arizona, Tucson, Arizona, USA.
[5]Space Sciences Laboratory, University of California, Berkeley, California, USA.

component rotates from southward to northward, the auroral oval contracts toward higher latitudes. Proton precipitation from the ring current may not change latitude, resulting in the appearance of a subauroral arc as the auroral oval contracts. An IMF B_y rotation from negative to positive will produce a similar effect. For this rotation the oval will shift from dusk to dawn, potentially exposing a subauroral proton arc on the duskside. Both IMF orientation changes have been observed to create duskside, long-duration subauroral arcs [*Burch et al.*, 2002]. The persistence of these arcs on the duskside has been linked to the cold plasmaspheric population on that side of the magnetosphere [*Burch et al.*, 2002; *Spasojević et al.*, 2004].

[7] Shorter-duration subauroral proton arcs have been associated with rapid increases in the solar wind dynamic pressure either through interplanetary shocks or pressure pulses [*Fuselier et al.*, 2001; *Zhang et al.*, 2003; *Hubert et al.*, 2003]. These transient arcs have several features that suggest their generation mechanism. They occur in association with rapid increases in dynamic pressure [*Fuselier et al.*, 2001], although the initial brightening of the arc can lag the brightening of the auroral oval [*Zhang et al.*, 2003]. They are not confined to the duskside [*Hubert et al.*, 2003]. The arcs are often separated from the auroral oval in latitude, usually by several degrees. Magnetic field lines that are equatorward of the auroral oval are mapped to the equatorial, outer magnetosphere inside the magnetopause. This is the general region of the equatorial ring current, and the precipitation in the arc consists of protons with ring current energies [*Hubert et al.*, 2003; *Zhang et al.*, 2003]. The arcs can occur under any solar wind IMF conditions, but they are best observed when the IMF is northward during the increase in dynamic pressure [*Hubert et al.*, 2003].

[8] Several mechanisms have been proposed for the generation of these short-duration subauroral proton arcs [*Hubert et al.*, 2003; *Zhang et al.*, 2003]. To be consistent with the precipitating proton energy, all proposed mechanisms invoke some sort of pitch angle diffusion of ring current particles into the loss cone through wave-particle interactions. Candidate instabilities include the loss cone instability, field-aligned resonances, and the electromagnetic ion cyclotron (EMIC) instability [*Hubert et al.*, 2003]. Scattering by EMIC waves is particularly promising because these waves are common in the outer magnetosphere near noon and near dawn, even in the absence of a compression of the magnetosphere [*Anderson et al.*, 1992]. The ring current proton distributions can be near the threshold of the instability [*Anderson et al.*, 1996], and the waves are readily generated during compression events [*Anderson and Hamilton*, 1993]. Finally, the growth of the instability is suppressed by rapid pitch angle scattering, reducing the anisotropy of ring current protons (i.e., reducing the free energy source of the waves) [*Gary et al.*, 1994, 1995]. This rapid pitch angle scattering will force ring current protons into the atmospheric loss cone.

[9] While promising, the generation of subauroral proton arcs through the above EMIC wave-particle mechanism requires some detailed investigation. This or any other generation mechanism must be able to explain two characteristics of these short-duration proton arcs. First, these proton arcs are not confined to the duskside but can occur over a longitudinal extent centered at almost any local time on the dayside. Second, the arcs are often separated from the main auroral oval, with a significant gap in the precipitating protons between the arc and the oval. The protons that produce the dayside auroral oval emissions originate at or near the magnetopause. The occurrence frequency of EMIC waves also peaks close to the magnetopause [*Anderson et al.*, 1992], as does the ring current proton anisotropy [e.g., *Sibeck et al.*, 1987]. In contrast, the subauroral arc resides at the ionospheric foot point of magnetic field lines that cross the equatorial plane in the vicinity of geosynchronous orbit (i.e., well inside the magnetopause). There is little scattering of protons into the loss cone in the gap between the equatorial magnetopause and the mapped location of the subauroral arcs. Based solely on the increasing ring current proton anisotropy with increasing radial distance from the Earth, this gap is difficult to explain using the EMIC waves.

[10] This paper investigates these two features of the short-duration subauroral proton arcs produced by rapid changes in solar wind dynamic pressure. In section 2 the instrumentation used in the investigation is briefly described. In section 3 the IMAGE and solar wind observations are introduced using a single event as an example. In section 4 the IMAGE and solar wind observations from many events are used to demonstrate how proton arcs can be centered at almost any dayside local time. In section 5 the aspects of EMIC wave theory relevant to the investigation are described. In section 6, ring current and plasmasphere observations are introduced, and EMIC wave theory is applied to several events to demonstrate how proton arcs can occur detached from the auroral oval. Finally, in section 7 the observations are summarized and discussed.

2. Instrumentation

[11] Remote sensing auroral observations in this paper are from the spectrographic imager SI12 [*Mende et al.*, 2000] on the IMAGE spacecraft. This spectrograph images Doppler-shifted Lyman-alpha emissions and excludes emissions from the intense, geocoronal Lyman-alpha line at 121.6 nm. These Doppler-shifted emissions are produced by protons precipitating into the upper atmosphere that charge-exchange with upper atmospheric constituents. The newly created hydrogen atoms are moving away from the spacecraft, so the Lyman-alpha photons they emit are Doppler-shifted to longer wavelengths. As discussed in section 1, this paper focuses on the dayside precipitation produced by precipitating ring current protons with initial energies of $\sim$10 keV.

[12] Remote sensing plasmaspheric observations are from the EUV cameras [*Sandel et al.*, 2000] on the IMAGE spacecraft. These cameras produce images of 30.4 nm solar radiation that is resonantly scattered off of plasmaspheric He^+. The observed 30.4 nm intensity is a line-of-sight integral measure of the plasmaspheric He^+.

[13] In situ ring current and plasmaspheric observations are from the Magnetospheric Plasma Analyzers (MPA) [*Bame et al.*, 1993] on the Los Alamos National Laboratory (LANL) geosynchronous spacecraft. These electrostatic analyzers measure ion and electron distributions with energies from the spacecraft potential to $\sim$40 keV/e. The ion data are used to determine the in situ growth rate of EMIC
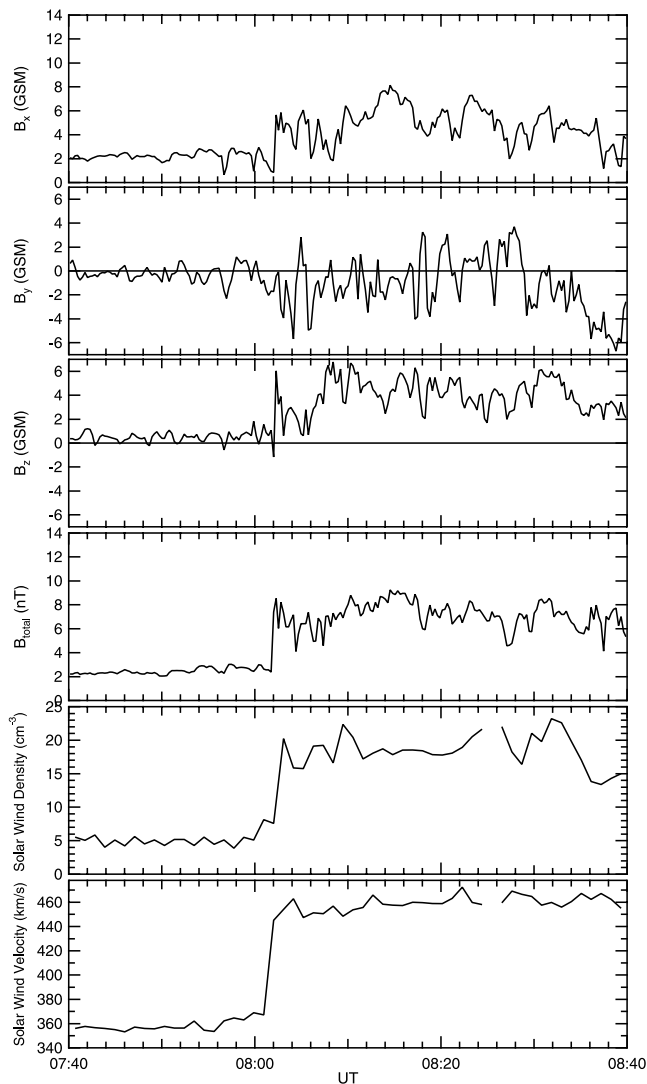
Figure 1. Magnetic field and plasma data from the ACE spacecraft on 25 October 2001. A strong interplanetary shock passed the spacecraft at 0802 UT. Magnetic field data are used to compute the shock normal angle. Solar wind velocity and density increase across the interplanetary shock, causing a significant compression of the magnetosphere ~50 min after the encounter of the shock by the ACE spacecraft.

waves at geosynchronous orbit, occasionally for several local times (using data from several spacecraft). To determine the growth rate of the waves, the hot proton temperature anisotropy, the plasma β (the ratio of particle energy to the magnetic field energy), and the cold plasma density are needed. Although there are no magnetometers on the spacecraft, the hot proton temperatures perpendicular and parallel to the background magnetic field direction are determined from the fully three-dimensional ion data and the assumption of gyrotropy. The directions perpendicular and parallel to the background magnetic field obtained from the ion observations are checked using the simultaneous electron observations (since electrons are also anisotropic in the outer magnetosphere). To determine the plasma β, the densities and temperatures from the electrostatic analyzers

are used, and magnetic field magnitude is estimated from the nearest GOES spacecraft (also in geosynchronous orbit). One of the features of the LANL MPA instruments is that they are typically at a negative potential. Thus the electrostatic analyzers also measure the in situ cold plasmaspheric ion population (with typical energies below 1 eV/e). These in situ observations of the cold plasmaspheric population have been compared to the remote sensing observations from the EUV cameras on IMAGE.

[14] Finally, in situ solar wind plasma and magnetic field observations are from the solar wind electron proton alpha monitor (SWEPAM) and the magnetic fields experiment on the ACE spacecraft. This spacecraft is located in the solar wind at the L1 Lagrange point (~237 R_E upstream from the Earth), resulting in time delays for solar wind propagation to the Earth's magnetopause of ~50 min.

3. Subauroral Proton Arc Example on 25 October 2001

[15] Figure 1 shows 1 hour of data from the ACE spacecraft from 25 October 2001. Data from the ACE magnetic fields experiment [*Smith et al.*, 1998] are shown in the first through fourth panels, and data from the ACE SWEPAM [*McComas et al.*, 1998] are shown in the fifth and sixth panels. At 0802 UT the ACE spacecraft observed the passage of a strong interplanetary shock. Across this shock the magnetic field increased and rotated, and the density and velocity increased. The dramatic increase in the solar wind density and the increase in the velocity resulted in a solar wind dynamic pressure increase of a factor of 5.5. From the ACE spacecraft location at the L1 point the interplanetary shock propagated to the Earth's magnetopause in ~50 min. The magnetopause was compressed, and effects of this compression were seen in the ionosphere starting at ~0853 UT.

[16] Figure 2 shows observations from the IMAGE spacecraft on 25 October 2001 and illustrates typical features of the subauroral proton arcs associated with dramatic increases in solar wind dynamic pressure. Figures 2a–2c show the proton auroral emissions from the SI12 imager remapped into geomagnetic coordinates (invariant latitude and magnetic local time (MLT)). The view is from over the north magnetic pole with noon at the top and dusk to the left. Figures 2d–2f show how these emissions map to the equatorial plane (see below in this section). The color bars for Figures 2a–2c and Figures 2d–2f are different and were chosen to highlight features in panels.

[17] The first effects of the interplanetary shock were seen in the ionosphere at 0853 UT (just before Figure 2a) as a brightening of the auroral oval. In Figure 2a the subauroral proton emissions are seen between about 11 and 15 MLT and between 65° and 70° invariant latitude. There is a clear separation between the subauroral arc, which peaks at ~68° invariant latitude, and the dayside auroral oval, which peaks at ~75° invariant latitude near noon (12 MLT). In Figures 2b and 2c the subauroral emissions move in both local time and latitude. At 0857 UT the emissions have split so that there are two arcs extending from 9 to ~11 MLT and from 12 to ~16 MLT. The duskside arc has moved to higher latitude and closer to the auroral oval. A gap between the subauroral emissions and the auroral oval is no longer
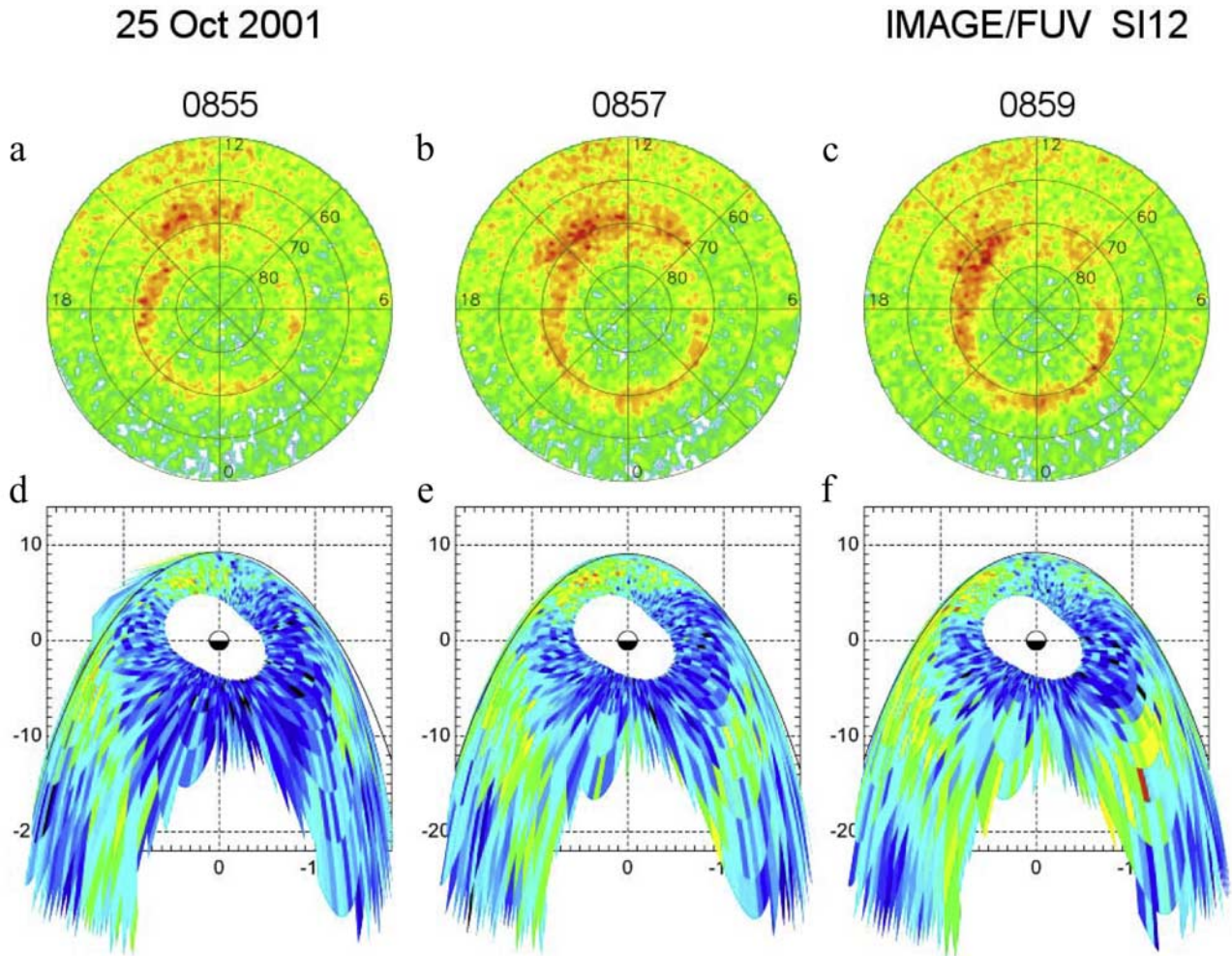
25 Oct 2001   IMAGE/FUV SI12

0855   **0857**   **0859**

Figure 2. IMAGE FUV data from 25 October 2001. (a–c) Doppler-shifted Lyman-alpha emissions remapped into invariant latitude and magnetic local time. Noon is to the top, and dusk is to the left. Auroral oval is at ∼75° invariant latitude, and the subauroral proton arc is at ∼68° invariant latitude between 11 and 15 MLT in Figure 2a. In Figures 2b and 2c the subauroral arc splits, with one part propagating toward dusk and the other propagating toward dawn. Both parts tend to merge with the auroral oval. (d–f) Mapping of the FUV emissions from the ionosphere to the GSM equatorial plane. In Figure 2d the subauroral proton arc maps to a region between about 11 and 15 MLT and about 5 and 8 R_E. In subsequent mappings the arc splits and propagates around the dayside outer magnetosphere.

discernable, except from about 15 to 16 MLT. By 0859 UT the separation between the dawnside and duskside arcs has increased, and these arcs have merged with the auroral oval. The duskside arc has a greater invariant latitude extent and is more intense than the dawnside arc. In the next two images (not shown) the subauroral emissions fade and are gone by 0905 UT.

[18] In Figures 2d–2f the emissions between 60° and 80° invariant latitude are mapped to the equatorial plane. To produce the mapped images, the corners of each pixel in this invariant latitude range were mapped from the ionosphere (assuming emissions at 100 km altitude) to the equatorial plane in the Tsyganenko 96 [*Tsyganenko*, 1995] model. The outer limit of the mapping from the high-latitude ionosphere to the equatorial plane is the magnetopause, which is compressed by the interplanetary shock from its nominal standoff distance of ∼10 R_E. The oval-shaped inner boundary in Figures 2d–2f is created by limiting the mapping to

invariant latitudes >60°. The auroral oval at 12 MLT maps tailward of −20 R_E on lobe field lines (which will be reconnected at high latitudes, forming the cusp [e.g., *Fuselier et al.*, 2002]). The duskside auroral oval between 70° and 75° invariant latitude and between 15 and 18 MLT maps to the duskside magnetopause just tailward of the terminator. In general, dayside pixels map to the dayside equatorial region with relatively little distortion, an indication that small changes in latitude result in correspondingly small changes in radial distance from the Earth. In contrast, pixels on the nightside map with significant distortion.

[19] In Figure 2d (corresponding to the FUV image at 0855 UT) the subauroral proton emissions are between 11 and 15 MLT and between 5.5 and 8 R_E. There is a clear peak in the emissions that occurs on the duskside, between the magnetopause and the inner boundary of the mapping. This peak is located near geosynchronous orbit (6.6 R_E). In the mapped image at 0857 UT the subauroral emissions split,

Table 1. Data for 18 Interplanetary Shocks Observed by the ACE Spacecraft That Were Associated With Subauroral Proton Arcs Observed by the IMAGE Spacecraft

Date	Shock Arrival Time at the ACE Spacecraft, UT	Shock x-y GSM Angle,[a] deg	Subauroral Arc Center,[a] deg
8 June 2000	0840:30	10.3	30
23 June 2000	1226:00	89.5	60
13 July 2000	0917:30	87.8	30
11 Aug. 2000	1810:30	6.6	7
14 Aug. 2000	2135:30	−62.9	−30
15 Sept. 2000	0407:00	−89.9	−6
17 Sept. 2000	2343:30	−6.7	27
28 Oct. 2000	0908:00	−15.8	−40
26 Nov. 2000	1124:00	−86.8	13
31 Jan. 2001	0723:00	−44.8	0
18 April 2001	0004:30	2.2	11
17 Aug. 2001	1016:00	−30.9	−40
27 Aug. 2001	1919:00	26.8	22
21 Oct. 2001	1612:30	63.4	16
25 Oct. 2001	0802:30	35.7	24
19 Nov. 2001	1735:00	−11.2	32
18 March 2002	1236:30	50.8	0
23 April 2002	0415:00	−25.1	0

[a]Positive angles are duskside, and negative angles are dawnside.

moving to earlier and later magnetic local times and closer to the magnetopause. By 0859 UT the duskside emissions have merged with the magnetopause emissions, forming a broad region of emissions extending earthward from the magnetopause several Earth radii and from about 14 to 18 MLT. The fainter dawnside emissions have merged with the magnetopause between 8 and 11 MLT.

[20] Although the splitting and propagation of the subauroral emissions are features not discussed previously, the other features of the subauroral emissions shown in Figure 2 have been reported [*Hubert et al.*, 2003; *Zhang et al.*, 2003]. In particular, the emissions are not confined to the duskside, they are clearly separated from the auroral oval (at least initially), they appear approximately in association with the arrival of a solar wind dynamic pressure pulse, and they last of the order of 10 min.

4. Local Time Dependence of Subauroral Emissions

[21] The subauroral emissions in Figure 2 initially appear on the duskside. Similar events with peak emissions occurring initially at noon and on the dawnside have been reported previously [*Hubert et al.*, 2003]. To investigate the local time occurrence of the emissions, solar wind data from ACE and IMAGE were surveyed from June 2000 (shortly after science operations began on IMAGE) to October 2002. During this period, there were 18 interplanetary shocks similar to the one shown in Figure 1 that had associated subauroral emissions like those in Figure 2. There were more interplanetary shocks and other sudden increases in dynamic pressure in the solar wind during this period. Not all of these sudden increases in solar wind dynamic pressure had subauroral emissions associated with them [see also *Zhang et al.*, 2003]. Although interesting and potentially important for understanding the creation of these subauroral emissions, the association between the type of solar wind disturbance and presence or absence of sub-

auroral emissions is not considered here. Rather, the focus here is on interplanetary shocks (where the shock normal can be computed) that are associated with subauroral emissions. Table 1 lists the 18 interplanetary shocks used in this study.

[22] Shock normals were computed for the 18 shocks in Table 1 using the minimum variance technique [e.g., *Seon*, 1998]. Figure 3 compares the orientation of the shock normal with respect to the GSM x-y plane (keeping the x direction of the normal positive, toward the Sun) to the location of the peak emissions in the subauroral arcs mapped to the GSM equatorial plane. Although there is not a strong correlation between these two angles, there is a clear preference for subauroral arcs to peak on the duskside (dawnside) when the shock normal has a positive (negative) Y_{GSM} component. The example in Figure 2 is included in Table 1 and in Figure 3. For this event the shock normal in the x-y GSM plane was at an angle of $+35°$ relative to the Earth-Sun line (i.e., the shock arrived on the duskside of the magnetopause first) and the subauroral emissions in Figure 2d peak on the duskside at $24°$ relative to the Earth-Sun line.

5. EMIC Wave Theory

[23] Figure 3 suggests that the initial local time occurrence of the subauroral emissions is determined entirely by properties of the pressure pulse or shock in the solar wind. Under the hypothesis that EMIC waves are a likely mechanism for the precipitation of the protons that create the subauroral emissions, this section presents relevant
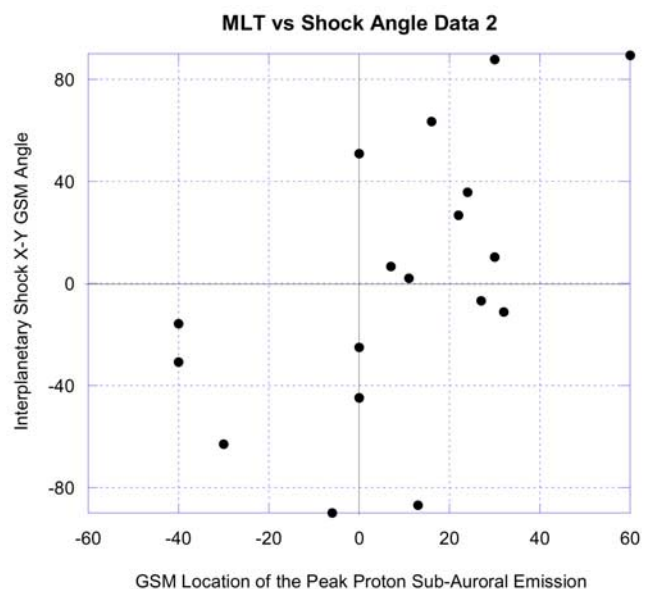

Figure 3. Interplanetary shock normal angle in the x-y GSM plane versus the GSM location of the peak in the proton subauroral emissions. Although the correspondence is not one-to-one, there is a clear tendency for subauroral emissions to peak on the duskside (dawnside) when the shock normal has a positive (negative) Y_{GSM} component. That is, shocks that arrive at the duskside (dawnside) magnetopause tend to create subauroral proton arcs that peak on the duskside (dawnside).

theoretical properties of the electromagnetic proton cyclotron anisotropy instability. These properties will be used in section 6, which discusses the latitudinal dependence of the subauroral emissions.

[24] The EMIC instability is driven by the temperature anisotropy ($A_h = T_{\perp h}/T_{\parallel h} - 1$) of the hot ring current proton distribution in the outer magnetosphere. In the duskside magnetosphere a process known as drift shell splitting causes these proton distributions to become increasingly anisotropic as they propagate from the nightside around the duskside to the dayside [e.g., *Sibeck et al.*, 1987]. In drift shell splitting, protons with small pitch angles preferentially drift to lower L shells on the dayside while those with large pitch angles drift to higher L shells. The result is a proton population whose anisotropy increases with increasing L shell in the subsolar and duskside magnetosphere. Compression of the magnetosphere due to the arrival of a solar wind pressure pulse should enhance this anisotropy to some degree throughout the dayside magnetosphere [*Anderson and Hamilton*, 1993].

[25] The proton temperature anisotropy is the free energy source for the EMIC instability. This instability has maximum growth rate at propagation parallel or antiparallel to the background magnetospheric magnetic field, so that protons are predominantly pitch angle scattered by the wave. Wave-particle interactions strongly scatter particles only when the anisotropy is sufficiently strong to excite the instability. This pitch angle scattering acts to reduce the free energy source and, when the anisotropy is reduced below a certain level, the instability is quenched.

[26] Since the proton temperature anisotropy is the free energy source, the growth rate of the EMIC instability is a function primarily of the proton temperature anisotropy and the proton β [e.g., *Gary*, 1993]. In the outer magnetosphere, there are typically two distinct proton populations, one hot and one cold. If the hot population is represented by a Maxwellian and $T_h \gg T_c$, then the maximum growth rate of the EMIC instability is primarily a function of the anisotropy A_h, the hot plasma beta, $\beta_{\parallel h}$, and the cold plasma density n_c. Here, $\beta_{\parallel h}$ is the ratio of hot plasma thermal energy to magnetic energy equal to $8\pi n_h T_{\parallel h}/B_o^2$ (n_h is the hot proton density, $T_{\parallel h}$ is the hot proton temperature parallel to the background magnetic field, and B_o is the background magnetic field magnitude). The n_c/n_h ratio changes the growth rate by changing the cyclotron resonance velocity of the hot protons. Linear theory calculations [e.g., *Cornwall et al.*, 1970; *Perraut and Roux*, 1975; *Gomberoff and Cuperman*, 1982; *Anderson et al.*, 1992] show that the cold plasma has little effect on the maximum growth rate at $n_c/n_h < 0.1$. For higher cold plasma densities ($n_c/n_h > 0.1$), including conditions typically found in the outer magnetosphere, the maximum growth rate increases with increasing n_c/n_h up to some value of the relative cold plasma density that depends on $\beta_{\parallel h}$. Still larger values of n_c/n_h lead to a decrease in the maximum growth rate.

[27] The location of the precipitation in the ionosphere depends critically on how and where the growth rate of the EMIC instability increases in the equatorial outer magnetosphere. As discussed above in this section, the growth rate depends on A_h, $\beta_{\parallel h}$, and n_c/n_h. In an adiabatic compression of the magnetosphere the temperature anisotropy, hot and cold plasma densities, perpendicular temperature, and mag-

netic field can all increase. It is the competition between the cold plasma density and the other factors that will determine where in the equatorial magnetosphere the EMIC instability will go unstable, rapidly scatter particles into the loss cone, and produce ionospheric precipitation.

6. Radial Dependence of Subauroral Emissions

[28] To investigate the relative importance of changes in A_h, $\beta_{\parallel h}$, and n_c in the growth of EMIC waves in the magnetosphere, in situ measurements of the ring current and plasmasphere from the Los Alamos geosynchronous spacecraft are used (and, for the magnetic field magnitude the magnetometer measurements from the nearest GOES spacecraft are used).

[29] One of the important assumptions in the determination of the EMIC growth rate is that the outer magnetospheric plasma consists of two populations, a hot ring current component and a cold, plasmaspheric population. Typically, proton distributions in the outer magnetosphere are more complex, often consisting of two or more hot components with different characteristic energies [e.g., *Anderson et al.*, 1996]. The lower energy component has a temperature of $\sim 10 - 20$ keV/e, while the higher-energy component can have temperatures above 40 keV/e. Despite its lower density when compared to that of the lower energy component, the higher-energy proton component can contribute as much as half of the total growth rate of the EMIC instability [*Anderson et al.*, 1996].

[30] The MPAs on the Los Alamos spacecraft measure ion energies (E/Q) from the spacecraft potential to 40 keV/e. Thus the analyzers cover the cold population and the lower energy ring current component well. The higher-energy component is measured by the Synchronous Orbit Particle Analyzers on the spacecraft. Unfortunately, the temperature anisotropy is not a normal data product derived from these energetic particle telescopes.

[31] By computing A_h and $\beta_{\parallel h}$ using only the lower energy component of the proton distribution measured by the MPAs, the absolute value of the growth rate of the EMIC waves could be underestimated by about a factor of 2. However, the interest here is on the relative changes in A_h and $\beta_{\parallel h}$, and the growth rate as an interplanetary shock or pressure pulse compresses the magnetosphere. Thus as long as the higher-energy proton component does not change dramatically during the compression of the magnetosphere, the relative changes in A_h and $\beta_{\parallel h}$ will be reasonably well determined from the MPA data. To minimize the effect of the higher-energy proton component on the relative changes in A_h and $\beta_{\parallel h}$, events were selected where the total energetic (from 50 to 200 keV/e) proton fluxes had little variation (less than a factor of 2) before and after the magnetospheric compression.

[32] Table 2 shows 11 events used to test the EMIC wave mechanism and the relative importance of changes in A_h and $\beta_{\parallel h}$ in producing EMIC wave growth. To identify a candidate event, subauroral proton arcs were mapped from the ionosphere to the equatorial magnetosphere using the same procedure described in section 3 that produced the mapping of the 25 October 2001 event (Figure 2). The locations of the Los Alamos geosynchronous spacecraft were checked to determine if any were in the mapped precipitation

Table 2. Plasma Parameters at Geosynchronous Orbit for Subauroral Proton Arc Events[a]

Date	Event Time at IMAGE	LANL Spacecraft	Spacecraft MLT	A_h Before	$\beta_{\parallel h}$ Before	n_h/n_c Before	γ_{max}/Ω_p Before	A_h After	$\beta_{\parallel h}$ After	n_h/n_c After	γ_{max}/Ω_p After
14 June 2000	1435	1991-080	15.2	0.53	0.153	0.55	7.5e-05	0.62	0.119	0.30	0.00061
13 July 2000	0955	1991-080	10.7	0.46	0.0821	0.08	0.00027	0.55	0.0668	0.09	0.00041
15 Sept. 2000	0453	1994-084	11.6	0.40	0.198	0.08	0.0012	0.59	0.255	0.28	0.0039
19 Sept. 2000	0720	1994-084	14.2	0.28	0.134	0.21	1.4e-08	0.37	0.130	0.15	2.6e-05
8 Nov. 2000	0614	1994-084	13.1	0.30	0.200	0.25	1.4e-06	0.29	0.267	0.39	7.4e-07
18 April 2001	0045	1991-080	13.3	0.54	0.0904	0.09	0.00090	0.54	0.138	0.10	0.0021
11 Sept. 2001	1558	01A	16.3	0.28	0.132	0.05	0.00013	0.38	0.119	0.03	0.0011
25 Oct. 2001	0855	97A	13.5	0.46	0.131	0.38	1.2e-05	0.47	0.179	0.06	0.0028
25 Oct. 2001	0855	1994-084	15.9	0.40	0.135	0.10	0.00030	0.45	0.194	0.06	0.0029
25 Oct. 2001	0855	01A	9.4	0.64	0.138	0.05	0.0054	0.63	0.192	0.04	0.0074
12 Dec. 2001	1345	01A	14.2	0.32	0.179	0.03	0.0011	0.37	0.167	0.02	0.0021

[a]Read 7.5e-05 as 7.5×10^{-5}, and so on, for all similar entries. LANL is Los Alamos National Laboratory.

region. If data were available in the mapped region, then the higher-energy proton data were checked to make sure the total flux above 50 keV did not change by more than a factor of 2. The 25 October 2001 compression event was particularly good in all aspects because there were three Los Alamos spacecraft located at different local times (Table 2) and all were in the broad region of precipitation observed over the 10 min lifetime of the event (Figure 2). These observations were considered as separate events in Table 2, even though they come from the same magnetospheric compression interval.

[33] Using the plasma conditions 10 min before the compression and immediately following the compression observed at the Los Alamos spacecraft, A_h, $\beta_{\parallel h}$, and the maximum growth rate were computed. The MPA data have a resolution of 1 min and, unless there were significant fluctuations in the density and/or temperature before or immediately after the compression, the highest time resolution data were used. If there were significant fluctuations in these parameters, then a three spectrum average was used.

[34] Most of the events in Table 2 support the EMIC wave generation mechanism described in section 5. For 10 of the 11 events the change in plasma conditions led to an increase in the instability growth, as shown in the comparison of the two columns representing the maximum growth rates (γ_{max}/Ω_p) before and after the magnetospheric compression. For only one event (8 November 2000) the relative change in the growth rate was small and in the direction of increasing stability.

[35] To understand how changes in local parameters lead to changes in the instability growth rate, two systematic studies were performed. These studies started with parameters from Table 2 for the 10 cases where the growth rate increased as a result of the compression. In the first study, two of the three parameters (A_h, $\beta_{\parallel h}$, n_c) were fixed at their values measured before the compression, while the third parameter was changed to its value measured after the compression. The result of this study showed that the change in A_h makes the largest contribution to the increase in the growth rate in 6 of the 10 events. In three remaining events the change in $\beta_{\parallel h}$ makes the largest contribution to the increase in the growth rate. In only one event the increase in n_c (or, equivalently, the decrease in n_h/n_c) makes the largest contribution to the increase in the growth rate. Thus under local conditions at geosynchronous orbit the

relative change in the cold plasma density was not a major factor in the enhancement in the growth rate.

[36] The second study investigated the role that the n_c plays in the radial dependence of the growth rate after the compression. Although the change in n_c does not contribute to the growth rate increase locally at geosynchronous orbit, the radial profile of n_c in the magnetosphere may play a significant role in determining the radial extent of the region where the EMIC waves are unstable after the magnetospheric compression. Typically, there is significant cold plasma at intermediate distances from the Earth (e.g., inside geosynchronous orbit), and the cold plasma density decreases rapidly at the plasmapause, further from the Earth. Such a density profile might cause the EMIC instability to be driven above marginal stability at intermediate distances from the Earth and not further from the Earth, even though the temperature anisotropy in the dayside outer magnetosphere increases with increasing radial distance from the Earth, and this anisotropy is the most important quantity in determining the EMIC growth rate. The limited region of precipitation resulting from the control of the EMIC instability threshold by n_c would produce a subauroral arc that is separated from the auroral oval, as in Figure 2.

[37] The second systematic study was performed on the same 10 events in Table 2 as the first study. For this study, A_h and $\beta_{\parallel h}$ were fixed at their values observed by the Los Alamos spacecraft after the magnetospheric compression, and n_c was reduced to zero. In 8 of 10 cases the growth rate was stabilized (i.e., there was no longer positive growth of the instability), and in the last two cases the growth rate was reduced to $\gamma_{max}/\Omega_p < 4 \times 10^{-5}$ (well below the marginal instability threshold of $\gamma_{max}/\Omega_p = 10^{-3}$).

[38] Figure 4 shows how the reduction in the growth rate depends on n_h/n_c for one of the events (11 September 2001, see Table 2). For this representative event a factor of 3 reduction in n_c results in an order of magnitude decrease in the growth rate. This parametric study indicates that if A_h and $\beta_{\parallel h}$ were constant with increasing radial distance from the Earth then the plasma would be stable if the plasmapause were between the observation point at geosynchronous orbit and the magnetopause. To be sure, A_h should increase with increasing radial distance from the Earth. However, this increase is probably <50% and not nearly as large as the factor of 5–10 decrease in n_c across the plasmapause. Furthermore, in this parameter regime a linear increase in A_h results in a linear increase in the EMIC
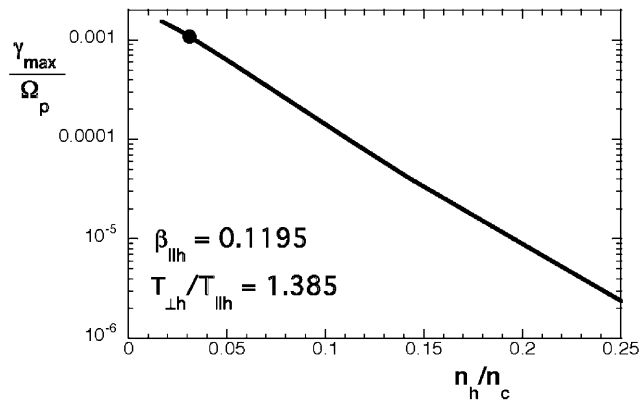
Figure 4. Maximum growth rate of the EMIC instability calculated from linear Vlasov dispersion theory as a function of n_h/n_c for the event on 11 September 2001. Hot proton parameters ($A_h = T_{\perp h}/T_{\parallel h} - 1$), n_h, and $\beta_{\parallel h}$ were fixed at their values after the magnetospheric compression (see Table 2). A factor of 3 decrease in the cold plasma density (which increases n_h/n_c from 0.03 to 0.09) results in a factor of 10 decrease in the maximum growth rate and lowers the growth rate below the instability threshold growth rate of ~ 0.001. A cold plasma density decrease of this magnitude could easily occur across the plasmapause.

growth rate, while a relatively small decrease in n_c leads to an exponential decrease in γ_{max}/Ω_p. Therefore it is likely that the gap in precipitation often seen between geosynchronous orbit and the magnetopause is produced by the cold plasma density profile.

[39] The cold plasma density profile is observable using the IMAGE EUV telescopes that image the Earth's cold plasmaspheric He$^+$. These telescopes have produced the first global images of the Earth's plasmasphere [*Sandel et al.*, 2001]. While these images provide the radial profile of the cold plasma density, there are two difficulties with applying these images to the study of subauroral arcs. The first difficulty is that the time resolution of the EUV images is 10 min. Since the time resolution is of the same order as the duration of the subauroral proton arc, it is not possible to compare the plasmasphere before and during the subauroral proton arc event. The second difficulty is that the 30.4 nm emissions are relatively weak at large distances from the Earth.

[40] Because of the weak 30.4 nm emissions it is usually not possible to obtain accurate cold plasma densities at L shells beyond $\sim 6-7$ R_E under nominal magnetospheric conditions. Thus the radial profiles of the cold plasma density obtained by EUV typically do not extend into the gap region between the magnetopause and geosynchronous orbit.

[41] Fortunately for this study, subauroral proton arcs are observed at very low latitudes on occasion, with a significant gap between the arc and the auroral oval emissions [*Hubert et al.*, 2003]. For these relatively rare events the region in the equatorial plane where protons are pitch angle scattered into the loss cone is at low L shells (i.e., very close to the Earth), and the gap, where scattering is not occurring, can be inside geosynchronous orbit. Figures 5a, 5c, and 5e show such an event. Figures 5a–5d have the same format as

Figure 2. For the event in Figures 5a, 5c, and 5e (14 June 2000) the subauroral arc extends to nearly 60° on the dawnside, and the gap between the emissions and the auroral oval is as large as 10° at 12 MLT. When mapped to the equatorial magnetosphere this subauroral arc is ~ 2 R_E from the Earth and extends only to ~ 5 R_E at 12 MLT. The result is a gap of nearly 4 R_E between the outer edge of the mapped subauroral arc and the subsolar magnetopause. Finally, Figure 5e compares the radial profile (centered at 12 ± 0.5 MLT) of the mapped FUV emissions with the EUV brightness. There is a decrease in the cold plasma density (i.e., the plasmapause) at ~ 3.8 R_E. Similarly, the mapped FUV emissions decrease between 4 and 4.5 R_E, or in the vicinity of the cold plasma density decrease. That is, within the resolution of the mapping and image, the outer edge of the mapped region of FUV emissions is associated with the decrease in the cold plasma density, identified as the plasmapause. (The plasmasphere for this event is located unusually close to the Earth, as are the mapped subauroral proton emissions. The final, relatively sharp decrease at $L = 6$ in the EUV brightness is the edge of the EUV image and illustrates the difficulty in using these images to study more typical subauroral proton arcs that map to the vicinity of geosynchronous orbit.)

[42] For this event, there were no Los Alamos geosynchronous spacecraft in the mapped emission region. However, one spacecraft was located at 16.9 MLT, outside the mapped emission region on the duskside. At this duskside location, both A_h and $\beta_{\parallel h}$ decreased when the magnetosphere was compressed. That is, the plasma in the vicinity of geosynchronous orbit on the duskside became more stable to the growth of EMIC waves. Also, the cold plasma density decreased during the magnetospheric compression, again indicating that, on the duskside in the vicinity of geosynchronous orbit, the plasma was stable to EMIC wave growth.

[43] The cold plasma does not always have a relatively steep gradient in the outer magnetosphere. Figures 5b, 5d, and 5f show a similar FUV-EUV comparison for an event on 18 April 2001 where the subauroral proton arc was not separated from the auroral oval. In this case, there is no gap between the magnetopause, and the FUV intensity decreases rapidly with decreasing L shell. The EUV intensity decreases smoothly with increasing L shell until ~ 6 R_E, where the poor statistics make it difficult to detect a sharp decrease in cold plasma density that might indicate the plasmapause. In this event the region of FUV emissions and the cold plasma density appear almost anticorrelated.

[44] For this event a Los Alamos geosynchronous spacecraft was in the mapped region of the emissions and relatively close to the magnetopause owing to the magnetospheric compression. The 18 April 2001 entry in Table 2 shows that the anisotropy was unchanged after the magnetospheric compression. However, $\beta_{\parallel h}$ increased, moving the plasma toward increasing instability. This event was one of the four in Table 2 where the change in n_h caused the increase in the EMIC growth rate. Thus for this event it was the increase in the hot plasma density and the hot plasma parallel temperature that caused $\beta_{\parallel h}$ to increase and the marginal stability condition of the EMIC instability to be exceeded. No sharp gradient was seen in the cold plasma
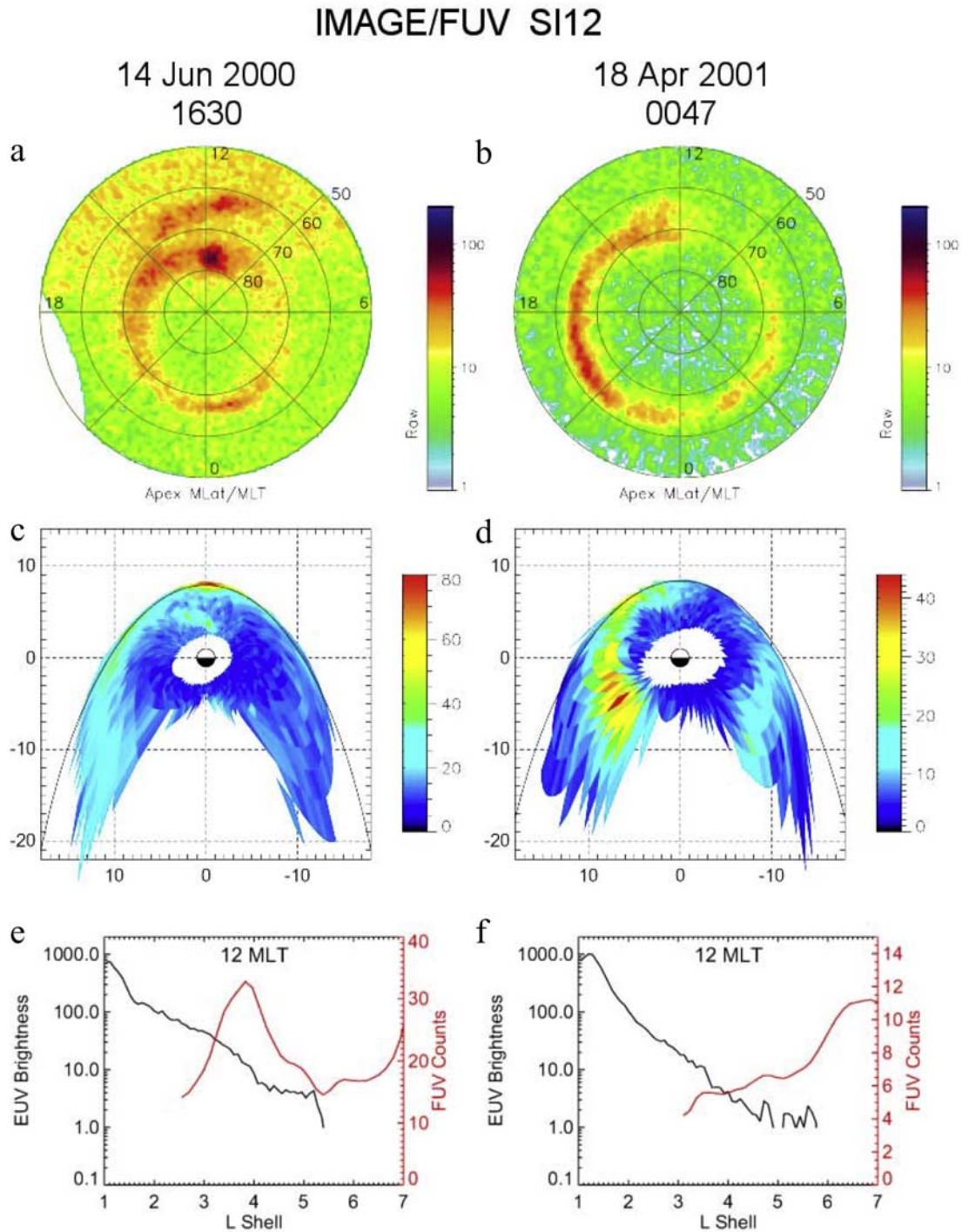
Figure 5. IMAGE FUV and EUV data from two subaurora proton events. (a–d) Similar to those in Figure 2. (e and f) Comparison of cuts in the proton precipitation mapped to the equatorial plane with similar cuts in the EUV He$^+$ emissions (proportional to the plasmaspheric density assuming a constant He$^+$/H$^+$ density ratio). For the event on 14 June 2000 (Figures 5a, 5c, and 5e) the subauroral proton arc is separate from the higher-latitude auroral oval. Mapped to the equatorial plane, this arc occurs quite close to the Earth and extends from noon to the duskside. The sunward edge of the precipitation at 12 MLT compares well with the decrease in the plasmaspheric density at the plasmapause at 3.8 R_E. (The drop in the EUV brightness at 6 R_E is the edge of the EUV image). Thus the growth of the EMIC waves that scatter the protons is controlled by the cold plasma density profile for this event. For the event on 18 April 2001 (Figures 5b, 5d, and 5f), there is no gap between the subauroral proton arc and the auroral oval emissions. These emissions extend inward from the magnetopause to inside geosynchronous orbit on the duskside. For this event the cold plasma density appears anticorrelated with the mapped proton emissions. Thus for this event the EMIC wave growth is not dominated by the cold plasma density.

density in the outer magnetosphere, and the arc was not separate from the auroral oval.

7. Discussion and Conclusions

[45] In this paper, the solar wind and magnetospheric drivers for two features of subauroral proton arcs were investigated. For the first feature, the local time occurrence in the peak of the subauroral emissions, the orientation of the solar wind pressure pulse or shock front plays an important role. Figure 2 shows that the orientation of the shock front is associated with the side of the magnetosphere where the peak of the mapped subauroral emissions is located. The correlation is far from perfect, but shock fronts that impact the duskside (dawnside) magnetosphere first tend to produce regions of enhanced pitch angle scattering on the duskside (dawnside).

[46] There are several reasons why the correlation is not expected to be perfect. The relatively short duration of the subauroral arcs and their propagation to later and earlier local times (Figure 2) could reduce the correlation between the shock front and the local time occurrence of the peak in the emissions. Since the FUV imager makes a $\sim$5–10 s snapshot of the auroral emissions every 2 min, and the events typically last only 10 min, the initial precipitation may be missed, and the subauroral arc might have already moved to earlier (or later) local times by the time the first image is obtained. For example, the peak intensity of the emissions in Figure 2 moves almost 1 hour in magnetic local time (i.e., 15°) from Figures 2a and 2d to Figures 2b and 2e.

[47] Another reason why the correlation is not expected to be perfect is the uncertainty in the shock normal angle. The minimum variance technique is correctly applied using asymptotic conditions upstream and downstream from the shock. However, the precipitation occurs over a short time period in the first $\sim$10 min of the shock arrival at the magnetopause. The orientation of the downstream field just after the shock arrival is typically somewhat different from the asymptotic orientation (see Figure 1). It is estimated that this can contribute to uncertainties in the shock normal angle of the order of ±20°.

[48] Finally, the correlation in Figure 3 is not expected to be perfect because of the asymmetric distribution of cold plasma and hot proton anisotropy in the dayside magnetosphere. Figure 3 shows that it is sometimes the case that the subauroral proton arcs occur on the duskside, even when the interplanetary shock arrives first on the dawnside. There is no corresponding tendency for arcs on the dawnside when the interplanetary shocks arrive first on the duskside. Figure 2 shows that as the emissions propagate around the magnetosphere the dawnside emissions tend to fade more rapidly than the duskside emissions.

[49] Two effects favor EMIC wave growth on the duskside when compared to the dawnside. First, the cold plasma is typically further away from the Earth on the duskside, resulting in a region of higher EMIC growth rate further from the Earth on the duskside. Second, even in the absence of a magnetopause compression the hot ring current proton anisotropy peaks on the duskside near the magnetopause [e.g., *Anderson et al.*, 1996]. Combining this duskside preference with the possibility that the initial peak in the

emissions might be missed by the FUV imager suggests that there is a higher probability of observing a peak in the emissions on the duskside than on the dawnside.

[50] The cold plasma density in the magnetosphere also appears to play an important role in the second feature of subauroral proton arcs: the latitudinal extent and the gap between the subauroral arc and the main auroral oval. Hot plasma parameters (A_h and $\beta_{\|h}$) are the primary drivers of the instability at geosynchronous orbit. However, a decrease in n_h/n_c reduces the growth rate of the EMIC instability (Figure 4), thereby reducing the proton scattering and the subsequent proton precipitation. Figure 4 indicates that, if an observer were to move to higher L shells beyond the plasmapause, there would be a dramatic reduction or stabilization of the proton cyclotron instability and a quenching of the precipitation.

[51] Figure 5e illustrates this point. It shows that the gap between the mapped proton precipitation and the magnetopause is related to the drop of the cold plasma density at the plasmapause observed by the EUV cameras. Thus even though A_h increases with radial distance from the Earth [e.g., *Sibeck et al.*, 1987], the gap in the precipitation occurs because of the sensitive dependence of the instability threshold on the cold plasma density profile across the plasmapause.

[52] The cold plasma density does not dominate the EMIC wave growth for all cases. Figures 5b, 5d, and 5f show such an example. When there is no gap between the subauroral proton arc and the auroral oval, the mapped emissions appear to be anticorrelated with the cold plasma density profile. For this event the geosynchronous spacecraft observations (the 18 April 2001 entry in Table 2) in the region of the mapped emissions showed that the EMIC wave growth rate increased because of an increase in $\beta_{\|h}$ primarily through an increase in the hot plasma density.

[53] These results suggest that the gap between the subauroral arcs and the auroral oval is directly related to the presence of a plasmapause in the outer magnetosphere. Even though the temperature anisotropy increases with increasing radial distance from the Earth [*Sibeck et al.*, 1987; *Anderson et al.*, 1992; *Anderson and Hamilton*, 1993], the decrease in the cold plasma density at the plasmapause typically determines the sunward extent of the precipitation region for the subauroral proton emissions.

[54] Although the plasmapause plays an important role in the events studied here, a statistical study of in situ magnetic field data showed that there is no evidence of an increase in the occurrence frequency of EMIC waves at the nominal location of the plasmapause [*Anderson et al.*, 1992]. The apparent contradiction between the present study and the previous statistical study can be understood by considering the transient nature of the subauroral proton arcs. To show up in a statistical study of in situ data, the spacecraft observations of EMIC waves must be made at the plasmapause at the time of a compression of the magnetosphere. The probability of this occurring is small, so the statistical study does not reflect the transient conditions of the dayside outer magnetosphere just after a magnetospheric compression.

[55] A similar EMIC wave mechanism for producing longer-duration subauroral proton arcs has been suggested [*Burch et al.*, 2002]. In this instance the subauroral proton

arc on the duskside is exposed by a rotation of the interplanetary magnetic field. These arcs have a duration on the order of an hour. Consistent with the importance of the cold plasma density in the generation of EMIC waves it has recently been demonstrated that the sunward edge of a long-duration subauroral proton arc is closely associated with the plasmaspheric plume on the duskside [*Spasojević et al.*, 2004]. Thus the location of subauroral proton arcs appears to be controlled by the cold plasma density in the outer magnetosphere independent of their duration. This result also does not contradict large statistical studies of EMIC waves in the outer magnetosphere because, although the subauroral proton arc persists for a long time (hours), the occurrence frequency is low and requires certain solar wind conditions (e.g., a rotation in the interplanetary magnetic field).

References

Anderson, B. J., and D. C. Hamilton (1993), Electromagnetic ion cyclotron waves stimulated by modest magnetospheric compressions, *J. Geophys. Res.*, *98*, 11,369.

Anderson, B. J., R. E. Earlandson, and L. J. Zanetti (1992), A statistical study of Pc 1–2 magnetic pulsations in the equatorial magnetosphere: 1. Equatorial occurrence distributions, *J. Geophys. Res.*, *97*, 3075.

Anderson, B. J., R. E. Denton, G. Ho, D. C. Hamilton, S. A. Fuselier, and R. J. Strangeway (1996), Observational test of local proton cyclotron instability in the Earth's magnetosphere, *J. Geophys. Res.*, *101*, 21,527.

Bame, S. J., D. J. McComas, M. F. Thomsen, B. L. Baraclough, R. C. Elphic, J. P. Glore, J. T. Gosling, J. C. Chavez, E. P. Evans, and F. J. Wymer (1993), Magnetospheric plasma analyzer for spacecraft with constrained resources, *Rev. Sci. Instrum.*, *64*, 1026.

Burch, J. L. (2000), IMAGE mission overview, *Space Sci. Rev.*, *91*, 1.

Burch, J. L., et al. (2002), Interplanetary magnetic field control of afternoon-sector detached proton auroral arcs, *J. Geophys. Res.*, *107*(A9), 1251, doi:10.1029/2001JA007554.

Cornwall, J. M., F. V. Coroniti, and R. M. Thorne (1970), Turbulent loss of ring current protons, *J. Geophys. Res.*, *75*, 4699.

Fuselier, S. A., et al. (2001), Ion outflow observed by IMAGE: Implications for source regions and heating mechanisms, *Geophys. Res. Lett.*, *28*, 1163.

Fuselier, S. A., H. U. Frey, K. J. Trattner, S. B. Mende, and J. L. Burch (2002), Cusp aurora dependence on interplanetary magnetic field B_z, *J. Geophys. Res.*, *107*(A7), 1111, doi:10.1029/2001JA900165.

Gary, S. P. (1993), *Theory of Space Plasma Microinstabilities*, Cambridge Univ. Press, New York.

Gary, S. P., M. B. Moldwin, M. F. Thomsen, D. Winske, and D. J. McComas (1994), Hot proton anisotropies and cool proton temperatures in the outer magnetosphere, *J. Geophys. Res.*, *99*, 23,603.

Gary, S. P., M. F. Thomsen, L. Yin, and D. Winske (1995), Electromagnetic proton cyclotron instability: Interactions with magnetospheric protons, *J. Geophys. Res.*, *100*, 21,961.

Gomberoff, L., and S. Cuperman (1982), Combined effect of cold H^+ and He^+ ions on the proton cyclotron electromagnetic instability, *J. Geophys. Res.*, *87*, 95.

Hubert, B., J. C. Gérard, S. A. Fuselier, and S. B. Mende (2003), Observation of dayside subauroral proton flashes with the IMAGE-FUV imagers, *Geophys. Res. Lett.*, *30*(3), 1145, doi:10.1029/2002GL016464.

Immel, T. J., S. B. Mende, H. U. Frey, L. M. Peticolas, C. W. Carlson, J.-C. Gearad, B. Hubert, S. A. Fuselier, and J. L. Burch (2002), Precipitation of auroral protons in detached arch, *Geophys. Res. Lett.*, *29*(11), 1519, doi:10.1029/2001GL013847.

McComas, D. J., S. J. Bame, P. Barker, W. C. Feldman, J. L. Phillips, P. Riley, and J. W. Griffee (1998), Solar wind electron proton alpha monitor (SWEPAM) for the Advanced Composition Explorer, *Space Sci. Rev.*, *86*, 563.

Mende, S. B., et al. (2000), Far ultraviolet imaging from the IMAGE spacecraft, 3, Spectral imaging of Lyman-α and OI 135.6 nm, *Space Sci. Rev.*, *91*, 287.

Mende, S. B., et al. (2001), Global observations of proton and electron auroras in a substorm, *Geophys. Res. Lett.*, *28*, 1139.

Ono, T., T. Hirasawa, and C. I. Meng (1987), Proton auroras observed at the equatorward edge of the duskside auroral oval, *Geophys. Res. Lett.*, *14*, 660.

Perraut, S., and A. Roux (1975), Respective role of the cold and warm plasma densities on the generation mechanism of ULF waves in the magnetosphere, *J. Atmos. Terr. Phys.*, *37*, 407.

Sandel, B. R., et al. (2000), The extreme ultraviolet imager investigation for the IMAGE mission, *Space Sci. Rev.*, *91*, 197.

Sandel, B. R., R. A. King, W. T. Forrester, D. L. Gallagher, A. L. Broadfoot, and C. C. Curtis (2001), Initial results from the IMAGE extreme ultraviolet imager, *Geophys. Res. Lett.*, *28*, 1439.

Seon, J. (1998), Determination of normal vectors for boundaries of plasmas based upon Rankine-Hugoniot relations estimated with a single spacecraft, *J. Astron. Space Sci.*, *15*, 11.

Sibeck, D. G., R. W. McEntire, A. T. Y. Lui, R. E. Lopez, and S. M. Krimigis (1987), Magnetic field drift shell splitting: Cause of unusual dayside particle pitch angle distributions during storms and substorms, *J. Geophys. Res.*, *92*, 13,485.

Smith, C. W., M. H. Acuna, L. F. Burlaga, J. L. Heureux, N. F. Ness, and J. Scheifele (1998), The ACE magnetic fields experiment, *Space Sci. Rev.*, *86*, 611.

Spasojević, M., H. U. Frey, M. F. Thomsen, S. A. Fuselier, B. R. Sandel, and U. S. Inan (2004), The link between a detached subauroral proton arc and a plasmaspheric plume, *Geophys. Res. Lett.*, *31*, L04803, doi:10.1029/2003GL018389.

Tsyganenko, N. A. (1995), Modeling the Earth's magnetospheric magnetic field confined within a realistic magnetopause, *J. Geophys. Res.*, *100*, 5599.

Zhang, Y., L. J. Paxton, T. J. Immel, H. U. Frey, and S. B. Mende (2003), Sudden solar wind dynamic pressure enhancements and dayside detached auroras: IMAGE and DMSP observations, *J. Geophys. Res.*, *108*(A4), 8001, doi:10.1029/2002JA009355.

———————————

E. S. Claflin and S. A. Fuselier, Lockheed Martin Advanced Technology Center, Space Physics Dept. ADCS B/255, 3251 Hanover Street, Palo Alto, CA 94304-1191, USA. (fuselier@spasci.com)

S. P. Gary and M. F. Thomsen, Space and Atmospheric Sciences Group, Los Alamos National Laboratory, Mail Stop D466, Group NIS-1, Los Alamos, NM 87545, USA.

B. Hubert, Laboratoire de Physique Astrophysique et Planetaire, Institut d'Atmospherique et de Geophysique, Université de Liège, Allee du 6 Aout, 17, Bat B5c, Liège B-4000, Belgium.

T. Immel, Space Sciences Laboratory, University of California, Berkeley, Grizzly Peak Blvd. at Centennial Dr., Berkeley, CA 94720-7450, USA.

B. R. Sandel, Lunar and Planetary Laboratory, University of Arizona, 1040 East 4th Street, Room 901, Gould-Simpson Building, Tucson, AZ 85721, USA.